THE JOURNAL OF PHYSICAL CHEMISTRY C
A JOURNAL OF THE AMERICAN CHEMICAL SOCIETY

pubs.acs.org/JPCC

Article

Mechanisms of Anisotropic Particle Deposition: Prolate Spheroid Layers on Mica

Maria Morga,* Małgorzata Nattich-Rak, Zbigniew Adamczyk,* Damian Mickiewicz, Mariusz Gadzinowski, and Teresa Basinska

Cite This: *J. Phys. Chem. C* 2022, 126, 18550−18559

Read Online

ACCESS | Metrics & More | Article Recommendations | Supporting Information

ABSTRACT: Anisotropic particle deposition was investigated using the streaming potential method complemented with the atomic force microscopy (AFM) determination of the absolute particle coverage. The polymer particles were synthesized using the stretching procedure with consecutive oxidation of surface hydroxyl groups and coupling of polyethyleneimine. The bulk particle physicochemical properties were characterized by scanning electron microscopy (SEM), dynamic light scattering, and laser Doppler velocimetry. The particles were positively charged in the pH range of 3−10, exhibiting a prolate spheroid shape with an axis ratio of five. Thorough AFM and in situ optical microscopy measurements yielded the adsorption kinetics of particles under the diffusion-controlled regime. The experimental data were adequately interpreted in terms of the random sequential adsorption model with the surface blocking function derived from the scaled particle theory. The root-mean-square (rms) parameter of the layers for a broad range of particle coverage was also determined and interpreted using the topographical model developed in this work. The experiments were complemented by the measurements of the streaming potential of particle layers under various ionic strengths and pHs. The ζ (zeta)-potential data acquired in this way enabled to determine the universal hydrodynamic function describing the dependence of the streaming potential on the particle coverage. The function was used to express the ζ-potential of surfaces covered by particles in terms of substrate rms. It was argued that the acquired results, in addition to being significant to basic science, can be exploited as useful reference systems for quantitative interpretation of bioparticle deposition on abiotic surfaces.

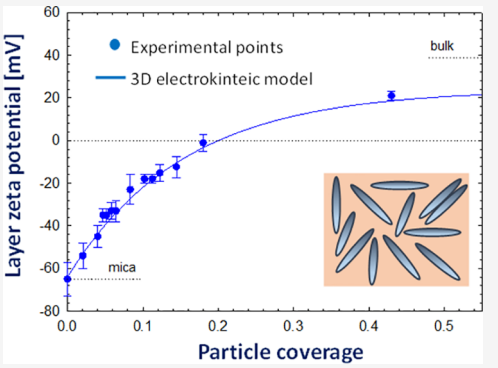

1. INTRODUCTION

Experimental studies on particle deposition kinetics furnish essential information about their interactions with interfaces, especially the adhesion strength, which is a crucial issue for colloid science, biophysics, medicine, soil chemistry, etc. This knowledge can be exploited for controlling and optimization of various practical processes such as filtration, flotation, protective coating formation, etc. Additionally, the results acquired for model colloid systems under well-defined transport conditions can serve as reference results for the interpretation of macromolecule and bioparticle adsorption phenomena, especially virus attachment to abiotic surfaces.

One should consider that the shape of metal nanoparticles,[1] carbon nanotubes,[2−4] silica particles,[5−8] synthetic polymer microparticles,[9−12] or macroions (polyelectrolytes),[13−16] can be approximated by prolate spheroid or cylinder shape. The anisotropic molecule shape is also common among biocolloids such as DNA fragments,[17−19] proteins,[20,21] viruses,[22,23] and bacteria[24,25] comprising the common bacterial strains such as *Escherichia coli*, *Sphingomonas alaskensis*, and *Hylemonella gracilis*.[26,27]

The nanoparticle and microparticle deposition kinetics was extensively studied by various experimental techniques comprising optical microscopy,[28] atomic force microscopy (AFM),[11,29−31] scanning electron microscopy (SEM),[11,32−34] ellipsometry,[35−37] reflectometry,[38,39] and the quartz crystal microbalance (QCM).[39−43]

However, few works were focused on measurements of anisotropic particle deposition kinetics.[41,44−47] In ref 41 the deposition of negatively charged spheroidal polystyrene particles at the poly-L-lysine modified silica sensor was investigated by QCM. The dependence of the initial deposition rate on ionic strength was determined. It was shown that in NaCl solutions the particle deposition rate was close to the theoretical value predicted from the convective-diffusion approach where the specific surface interactions were neglected. However, one should consider, that the interpretation of the QCM signal in the case of particle load is not unique because it significantly

Received: August 23, 2022
Revised: October 3, 2022
Published: October 20, 2022

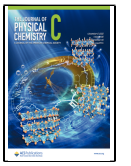

https://doi.org/10.1021/acs.jpcc.2c06028
J. Phys. Chem. C 2022, 126, 18550−18559

depends on sensor roughness, adhesion strength, and the overtone number.[43,48]

In ref 11 the deposition of negatively charged spheroidal particles on the PAH-modified mica substrate was determined by AFM.

However, these techniques cannot furnish reliable information about the electronic state of particle layers, especially their ζ (zeta)-potential as a function of the supporting electrolyte composition, ionic strength, and pH. This essential information can only be acquired using electrokinetic methods,[16,49−54] most frequently the streaming potential/streaming current, which enable in situ determination of the ζ-potential of particle layers. It is also worth mentioning that the electrokinetic measurements are particularly sensitive for the low coverage regime, where most other methods become of limited utility.

Therefore, the main goal of this work was to determine the mechanism of spheroidal particle deposition at the solid/electrolyte interface with the main focus on assessing the applicability of the streaming potential method. To increase the reliability of experiments, monodisperse and positively charged polymer particles were used, which promoted their irreversible adsorption on the negatively charged mica substrate. Electrokinetic measurements were supplemented by atomic force microscopy (AFM) that provided absolute particle coverage and the root-mean-square (rms) parameter of the layers. These complementary procedures enabled the determination of the universal function describing the dependence of the streaming potential/current on particle coverage. This function was used to express the ζ-potential of surfaces covered by particles in terms of substrate topography and roughness, which has not been done before in the literature.

One can also expect that the acquired results, in addition to being significant to basic science, can be exploited as useful reference systems for quantitative interpretation of protein and virus adsorption/desorption processes on abiotic surfaces.

2. EXPERIMENTAL SECTION

2.1. Materials. All chemical reagents comprising sodium chloride, sodium hydroxide, and hydrochloric acid were commercial products of Sigma-Aldrich and were used without additional purification. Ultrapure water was obtained using the Milli-Q Elix & Simplicity 185 purification system from Millipore.

As a model substrate for performing the particle deposition studies, muscovite mica was used. Mica sheets were freshly cleaved and used without further pretreatment in every set of experiments.

2.2. Synthesis of P(S/PGL) Spheroidal Microparticles. Synthesis of poly(styrene/α-*tert*-butoxy-ω-vinylbenzyl-polyglycidol) (PS/PGL) spheroidal microparticles is described in the Supporting Information. It was a tedious process consisting of four main steps (i) synthesis of α-*tert*-butoxy-ω-vinylbenzyl-polyglycidol (PGL) macromonomer, (ii) synthesis of P(S/PGL) microspheres using styrene and PGL macromonomer, (iii) preparation of spheroidal particles P(S/PGL) from the spherical ones applying the stretching of poly(vinyl alcohol) (PVA) films containing embedded P(S/PGL) microspheres. After completing these three steps one obtains uncharged spheroidal particles capped with a poly(vinyl alcohol) (PVA) surface layer. Finally, in the fourth step, positively charged particles were produced by a surface modification process consisting of selective oxidation of surface hydroxyl to carboxyl groups and the consecutive adsorption of polyethyleneimine (PEI).

Except for the spheroidal PS/PGL, the unstretched spherical particles of the same surface properties as the spheroids were also investigated as the reference system.

2.3. Methods. The chemical composition of the particle was characterized by X-ray photoelectron spectroscopy (XPS) experiments, performed using the PHI 5000 VersaProbe − Scanning ESCA Microprobe (ULVAC-PHI, Japan/USA) instrument at a base pressure below 5×10^{-9} mbar. The particle morphology and size distribution were characterized by scanning electron microscopy using a JEOL 5500LV apparatus (Akishima, Japan).

The diffusion coefficient was determined by dynamic light scattering (DLS) using the Zetasizer Nano ZS instrument from Malvern. The hydrodynamic diameter was calculated using the Stokes−Einstein relationship.[55]

The electrophoretic mobility of particles was measured by the laser Doppler velocimetry (LDV) technique using the same apparatus. The ζ-potential was calculated using the Ohshima equation considering the electric double-layer polarization effect (Supporting Information).[56]

The concentration of particles in the stock suspension was determined by densitometry and the dry mass method, described elsewhere.[31] Before each deposition experiment the stock suspension was diluted to the desired concentration, typically equal to 200−300 mg L^{-1} with pure NaCl solutions with the pH adjusted by the addition of either NaOH or HCl solutions.

The deposition kinetics of particles was determined using optical microscopy and the AFM method as previously described in ref 57. The former method enabled real-time and in situ investigations in the diffusion cell with a horizontal microscope arrangement. The deposition kinetics and the rms of particle layers were determined by the ex situ AFM method. Accordingly, the adsorption kinetic runs were stopped after discrete time intervals, the mica sheets were removed from the suspension and imaged under ambient conditions using an NT-MDT Solver BIO device with a SMENA SFC050L scanning head. The number of particles per unit area (typically 1 μm^2), denoted hereafter as N, was determined by direct counting of over a few equal-sized areas randomly chosen over the surface with the total number of particles about 2000.

The ζ-potential of bare and particle-covered mica was determined from the streaming potential measurements,[58] applying the Smoluchowski formula where the correction for the surface conductivity was considered.

All experiments have been performed at the temperature of 298 K.

The deposition kinetic runs derived from AFM were theoretically interpreted in terms of a hybrid approach where the bulk particle transport was described by the convective-diffusion equation with the nonlinear boundary condition derived from the random sequential model (a detailed description of this approach is given in Supporting Information).

3. RESULTS AND DISCUSSION

3.1. Bulk Substrate and Particle Characteristics. The (PS/PGL) particle dimensions were determined by SEM, a typical micrograph is shown in Figure 1. The particle length, denoted hereafter as $2a$ and width denoted as $2b$ were separately obtained by measuring the corresponding dimensions of ca. 200 particles using image analyzing software. It was determined in

https://doi.org/10.1021/acs.jpcc.2c06028
J. Phys. Chem. C 2022, 126, 18550−18559

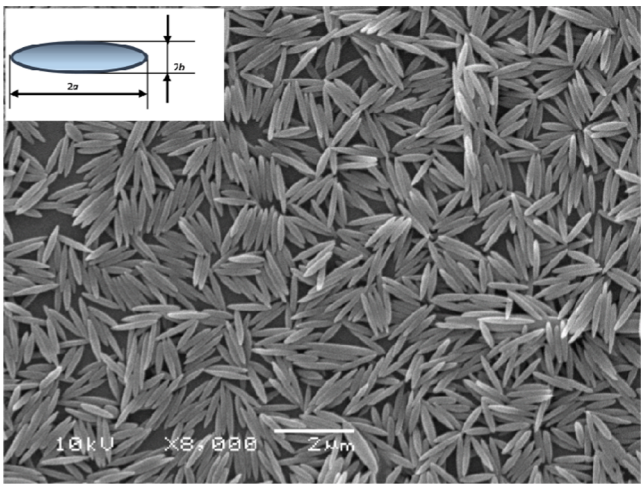

Figure 1. SEM image of the (PS/PGL) spheroidal particles. The inset shows a single spheroid with the definitions of its dimensions.

this way that the average length of particles was equal to 1010 ± 30 nm and the width was equal to 200 ± 10 nm. This indicates that the particles were fairly monodisperse and their shape could be well approximated by a prolate spheroid shape. Accordingly, their SEM axis ratio $\lambda = a/b$ was equal to 5.0.

Particle dimensions were also determined in an analogous way by AFM. The average length of particles was equal to 1020 ± 20 nm and the width was equal to 220 ± 10 nm. Accordingly, the AFM axis ratio of the spheroidal particles was equal to 4.6.

The diffusion coefficient of particles was determined by the DLS measurements. It was equal to 1.1 ± 0.02 × 10^{-8} cm^2 s^{-1} (for the pH range of 4−11 and the NaCl concentration range of 10^{-3} to 0.15 M). Using this value, the hydrodynamic diameter of the particles of 440 ± 20 nm was calculated using the Stokes−Einstein formula (Supporting Information).[55]

Thorough bulk electrokinetic characteristics of the spheroidal particles were acquired using LDV measurements, which directly yielded electrophoretic mobility. The ζ-potential was calculated from the Ohshima formula derived in refs 56, 59, 60 where the double-layer polarization effect was considered (Supporting Information). The dependence of the ζ-potential on pH for various ionic strengths fixed by NaCl is shown in Figure 2a. It was equal to 40 ± 2 mV for NaCl concentrations from 10^{-3} to 10^{-2} M and the pH range of 4−7. Only at pH above eight, the ζ-potential rapidly decreased attaining zero at pH 10.5. For ionic strength of 0.15 M, the ζ-potential was equal to 30 ± 2 mV for the pH range of 4−7.

Analogous measurements, presented in Supporting Information confirmed that the ζ-potential of spherical particles (used for the preparation of spheroids according to the stretching procedure) was equal to 43 ± 2 mV for NaCl concentrations from 10^{-3} to 10^{-2} M and a pH range of 4−7.

On the other hand, the dependence of the ζ-potential of mica on pH for various ionic strengths determined by the streaming potential measurements is shown in Figure 2b. The potential was strongly negative and monotonically decreased with pH. At pH 5.6 it was equal to −64 ± 4 and −80 ± 5 mV for NaCl concentrations from 10^{-2} to 10^{-3} M, respectively. The mica surface is characterized by the negative charge, ascribed to the isomorph substitution of silicon by alumina atoms in the lattice. The charge is neutralized by potassium ions built into a layered structure of the aluminosilicate. In aqueous solutions, the K^+ cations dissociate producing a negative charge of the mica surface.[61]

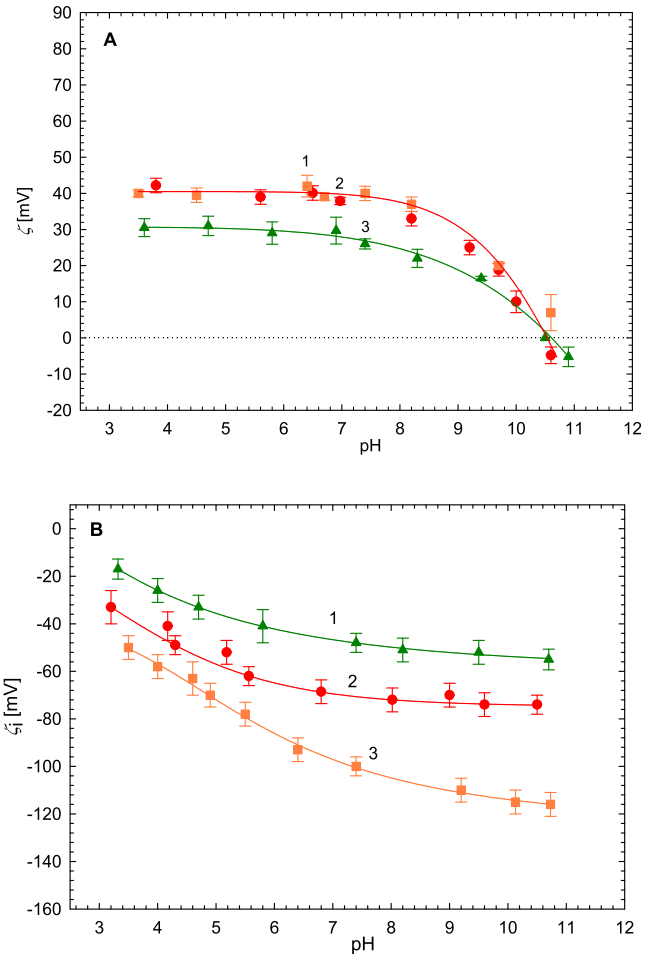

Figure 2. (A) Dependence of the bulk ζ-potential of spheroidal particles on pH derived from the LDV measurements on pH: 1 (yellow box) 10^{-3} M; 2 (red circle) 10^{-2} M; and 3 (green triangle) 0.15 M. (B) Dependence of the mica ζ-potential derived from the streaming potential measurements on pH: 1 (green triangle) 0.15 M; 2 (red circle) 10^{-2} M; and 3 (yellow box) 10^{-3} M. The points denote experimental results. The solid lines are the guide to the eye.

It should be underlined that because of the opposite sign of the ζ-potential of both the mica surface and spheroids, efficient and irreversible deposition of the particles could be realized without using modifications of the substrate surface by supporting macroion layers, as it was done in the previous work.[11]

3.2. Kinetics of Particle Deposition. The kinetics of spheroidal particle deposition on mica was initially studied to select appropriate conditions for the tedious streaming potential measurements. The measurements were performed under diffusion conditions, which enabled us to follow the kinetics in situ using optical microscopy. The results obtained by optical microscopy were compared with ex situ AFM measurements, which yielded, except for particle surface concentration, the root-mean-square of the layers, a parameter inaccessible by optical microscopy. A kinetic run was performed at pH 5.6, I = 10^{-2} M and the bulk suspension concentration of 200 mg L^{-1} is presented in Figure 3 as the dependence of the surface concentration (conveniently expressed as the number of particles on the square micrometer) on the square root of the

https://doi.org/10.1021/acs.jpcc.2c06028
J. Phys. Chem. C 2022, 126, 18550−18559

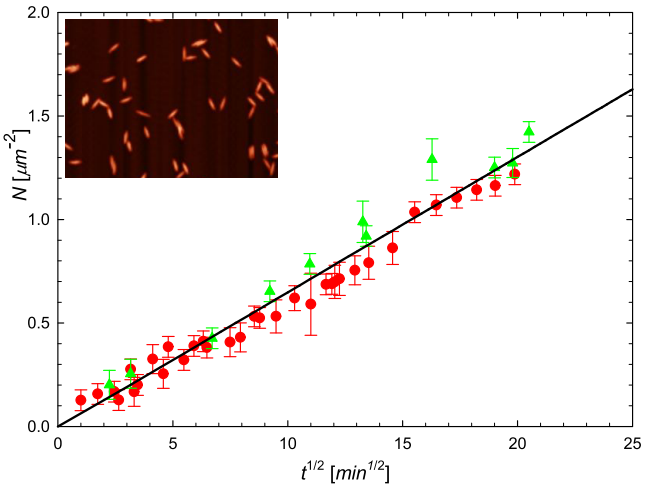

Figure 3. Kinetics of spheroidal particle deposition on mica expressed as the dependence of the particle surface concentration on the square root of deposition time. Experimental conditions; pH 5.6, $I = 10^{-2}$ M, and bulk suspension concentration of 200 mg L^{-1}. The green triangles show the results obtained by AFM and the red circles show the results obtained by in situ optical microscopy. The solid line presents the theoretical results derived from the general transport equation with the RSA blocking function. The inset shows the particle layer derived from AFM.

deposition time. As previously discussed,[11,51,62−64] this transformation is more convenient to analyze the kinetic runs performed under diffusion transport, compared to the natural time scale.

One can observe that the optical microscopy and AFM experimental results agree with each other within the error bounds and exhibit an almost linear dependence on the square root of the deposition time up to 20 $min^{1/2}$ (t = 400 min). This fact confirms the validity of the ex situ AFM determination of the particle coverage and in consequence the rms parameter. The experimental data were theoretically interpreted using the results derived from the hybrid random sequential (RSA) modeling (Supporting Information). In this approach, the coupling of the bulk particle transfer, driven by diffusion with the surface transfer, governed by the specific particle/particle interactions was considered in an exact way. The kinetics equation derived within the scope of this approach was numerically integrated, furnishing the particle adsorption kinetics. One can observe in Figure 3 that the RSA results derived assuming negligible particle desorption and a side-on orientation of the particles agrees with the experimental data for the entire range of the deposition time. This observation has practical significance because it confirms that the particle layer of a well-controlled coverage can be directly prepared within the streaming potential cell by appropriately adjusting the deposition time. In this way, precise in situ measurements of the particle layer streaming potential can be performed.

It is also worth mentioning that the AFM method makes it possible to quantitatively determine the root-mean-square parameter of particle layers, denoted by rms, whose square is defined as follows (Supporting Information)

$$\mathrm{rms}^2 = \frac{1}{S}\int_s (h(\mathbf{r}_s) - \overline{h})^2 \cdot \mathrm{d}\mathbf{r}_s = \frac{1}{S}\int_s h^2(\mathbf{r}_s)\cdot \mathrm{d}\mathbf{r}_s - \overline{h}^2 \quad (1)$$

where S is the projection area of the surface, $h(\mathbf{r}_s)$ is the local height of the surface profile measured relative to the reference plane located at h_0, $\mathbf{r}_s$ is the surface position vector, and $\overline{h}$ is the average height of a rough surface. The rms is calculated by taking the square root of eq 1.

The dependence of the rms determined using AFM software by eq 1 on the spheroid particle coverage $\Theta = \pi abN$ (where N is the particle surface concentration and a,b are the major and minor spheroid semi-axes) is shown in Figure 4.

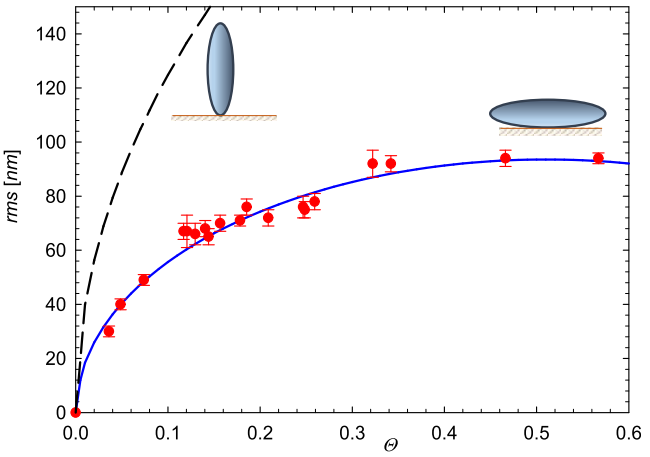

Figure 4. Dependence of the rms parameter of the spheroidal particle layers on mica on the coverage Θ. The points denote experimental results obtained from AFM; particle deposition conditions: pH 5.6, $I = 10^{-2}$ M NaCl, deposition time 1−24 h. The solid line shows the theoretical results calculated from eq 3 for the side-on deposition of particles and the dashed line shows the theoretical results calculated from eq 8 for the end-on deposition regime.

As can be seen, the rms parameter abruptly increases with the particle coverage attaining 50 nm for Θ = 0.1 and then, for Θ > 0.3, it approaches a plateau value of 90 nm, which corresponds to 41% of the shorter spheroid axis (determined by AFM), which suggests a side-on deposition mechanism of the particles. It should be underlined that the rms of the mica substrate was considerably lower, ca. 0.1 nm, therefore, it introduced a negligible error to these measurements. Analogously, the correction for the tip convolution effect was thoroughly analyzed in the Supporting Information. It was shown that the relative correction to the experimental values of the rms derived from AFM is given by

$$\sigma_{\mathrm{rms}} = \left(\frac{\pi}{2}\right)^{1/2}\left(\frac{\alpha}{360}\right)^{3/2} \quad (2)$$

where α is the tip cone angle.

One can calculate from eq 2 that the correction amounts to only 1.1% for the tip cone angle of 15°.

The experimental data shown in Figure 4 were interpreted in terms of the theoretical model formulated in the Supporting Information. It was shown that the average height and the rms of the layer of ellipsoidal particles are given by

$$\overline{h} = \frac{5}{3}\Theta\, c$$

$$\mathrm{rms} = \left(\frac{17}{6}\Theta\left(1 - \frac{50}{51}\Theta\right)\right)^{1/2} c \quad (3)$$

where c is the ellipsoid semi-axis in the direction perpendicular to the substrate surface.

https://doi.org/10.1021/acs.jpcc.2c06028
J. Phys. Chem. C 2022, 126, 18550−18559

For prolate spheroids, one has $c = b \neq a$ and for spheres $c = b = a$, with a corresponding to the sphere radius. Thus, for spheroids and spheres, eq 3 can be expressed in a more convenient form

$$\text{rms} = 0.8416\,[\Theta(1 - 0.980\Theta)]^{1/2}\, d_p \tag{4}$$

where $d_p = 2b$ is the shorter spheroid axis length or the sphere diameter.

For the low coverage range, eq 4 simplifies to

$$\text{rms} = 0.8416\,\Theta^{1/2}\, d_p \tag{5}$$

Equation 5 indicates that the rms of the spheroidal particle layers scale up as the square root of the particle coverage. Thus, using the rms factor derived from AFM, the particle coverage can be determined with a large sensitivity from the formula

$$\Theta = \frac{24}{17}\left(\frac{\text{rms}}{d_p}\right)^2 \tag{6}$$

Equation 4 indicates that the rms of spheroidal particle layer reaches a maximum at $\Theta = 0.51$ with the height equal to

$$\text{rms}_{mx} = 0.425\, d_p \tag{7}$$

For $\Theta > 0.51$, it is predicted from eq 4 that the rms monotonically decreases and attains $0.358\, d_p$ for $\Theta = \pi/4$, which corresponds to the regular closely packed monolayer of spheroids or spheres. However, such large coverages cannot be experimentally attained under the irreversible deposition regime governed by the RSA mechanism. The maximum (jamming) coverage theoretically predicted from the RSA modeling for hard spheroids with the axis ratio of 5 is equal to 0.536, compared to the value of 0.547 pertinent to spherical particles.[65]

For the end-on deposition of spheroids with the longer axis oriented perpendicularly to the substrate surface, eq 4 assumes the form

$$\text{rms} = 0.8416\left[\frac{b}{a}\Theta\left(1 - 0.980\frac{b}{a}\Theta\right)\right]^{1/2} d_p \tag{8}$$

where $d_p = 2a$.

As can be observed in Figure 4, the theoretical results calculated from eq 4 assuming the side-on deposition mechanism adequately reflect the experimental data for the entire range of coverage, in particular the position and the height of the rms maximum. In contrast, the theoretical results calculated from eq 8, shown by the dashed line in Figure 4, considerably overestimate the experimental data. Therefore, these results confirm the side-on adsorption mechanism of spheroids, which is energetically favored given the opposite charge of the particles and the mica substrate. This becomes evident if one compares the DLVO energy profiles for the side-on and the end-on orientation of the spheroid particles with a planar interface (Supporting Information). At distances smaller than the particle's shorter semi-axis, the net interaction energy ϕ is given by

$$\phi = -G_D\frac{A_{123}}{6\,h} + G_D\pi\varepsilon\left(\frac{kT}{e}\right)^2 f(\kappa h) \tag{9}$$

where the first and the second terms describe the van der Waals and the electric double-layer interactions, respectively, G_D is the geometrical Derjaguin factor[65] depending on the spheroid orientation, A_{123} is the Hamaker constant describing the van der Waals interaction of the particle through the electrolyte with the surface, h is the surface to surface distance, ε is the electric permittivity of the electrolyte, k is the Boltzmann constant, T is the absolute temperature, e is the elementary charge, and

$$f(\kappa h) = \left[(\overline{\zeta}_1^2 + \overline{\zeta}_2^2)\ln(1 - e^{-2\kappa h}) + 2\overline{\zeta}_1\overline{\zeta}_2\ln\frac{1 + e^{-\kappa h}}{1 - e^{-\kappa h}}\right] \tag{10}$$

$\overline{\zeta}_1 = \zeta_1\frac{e}{kT}$; $\overline{\zeta}_2 = \zeta_2\frac{e}{kT}$ are the normalized ζ-potentials of the substrate and the particle, respectively, $\kappa^{-1} = \left(\frac{\varepsilon kT}{2e^2 I}\right)^{1/2}$ is the electric double-layer thickness (I is the ionic strength of the electrolyte).

Considering that $G_D = a$ and b^2/a for the side-on and the end-on spheroid orientations, respectively, one can infer from eq 9 that the energy ratio for these limiting orientations is equal to[65]

$$\phi_{\parallel}/\phi_{\perp} = a^2/b^2 \tag{11}$$

where $\phi_{\parallel}$ and $\phi_{\perp}$ are the energies for the side-on and the end-on, orientations, respectively.

Note that eq 11 is valid for all particle/surface separations.

Thus, for our case, where $a/b = 5$, the energy profile and the minimum for the side-on orientation are 25 times deeper than those for the end-on orientation. Taking the ζ-potential data pertinent to our experimental system, i.e., $\zeta_1 = -64$ mV, $\zeta_2 = -40$ mV, and $I = 10^{-2}$ M ($\kappa = 3.05$ nm), and the Hamaker constant of $1.7\ 10^{-20}$ J[65] one can calculate that the energy minimum at the distance of 5 nm and the side-on orientation is equal to −540 kT, which is deep enough to assure a completely irreversible deposition. On the other hand, for the end-on orientation, the energy minimum depth is equal to −21 kT units. At a distance of 10 nm the energy minima are equal to −270 and −8 kT, for the side-on and the end-on orientations, respectively. Due to such a considerable difference in the interaction energy, the particles will tend to preferably deposit in the side-on orientation.

3.3. Electrokinetic Characteristics of the Particle Layers. The next series of experimental investigations was devoted to the electrokinetic characteristics of the particle layer applying the is situ streaming potential measurements. The procedure comprised the following steps: initially, the reference ζ-potential of bare mica was determined for a fixed ionic strength and pH, then the particle layer of a controlled coverage was deposited in the cell under the diffusion conditions. Afterward, the cell was flushed with pure electrolyte and the streaming potential was measured as a function of the hydrostatic pressure difference by a pair of reversible electrodes. Finally, the ζ-potential of the layer was calculated from the Smoluchowski equation. Except for the spheroidal particles, reference measurements for the spheres were performed applying the above procedure.

The stability of the particle layers was determined is separate experiments where the pure electrolyte was flushed through the cell over time up to 6 h. It was established that no change in the streaming potential occurred over this time period, which was interpreted as the lack of particle desorption.

The dependencies of the ζ-potential of the mica substrate on the spheroid particle coverage acquired at pH 5.6 and various ionic strengths are shown in Figure 5. For ionic strength of 10^{-2} M the results obtained for spheroids are compared to analogous results obtained for spheres under the same conditions (Figure 5A). As can be seen, the initially negative ζ-potential of mica

https://doi.org/10.1021/acs.jpcc.2c06028
J. Phys. Chem. C 2022, 126, 18550−18559

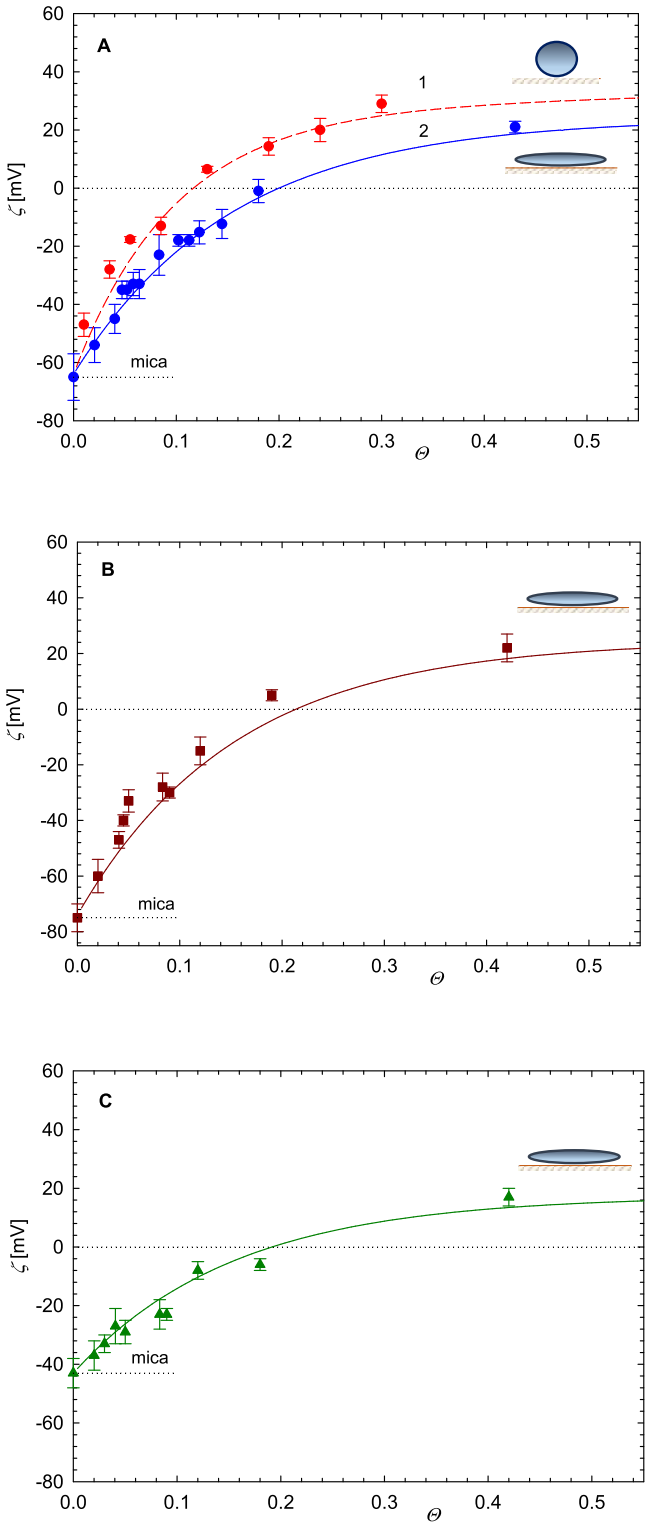

Figure 5. Dependence of the ζ-potential of mica on the coverage of particles acquired at pH 5.6. (A) Ionic strength 10^{-2} M. The points show the experimental data obtained by streaming potential measurements, the dashed red line (1) shows the theoretical results calculated for spheres from eqs 12 and 13; the solid blue line shows the theoretical results calculated from eqs 12 and 13 for spheroids. (B, C) Dependence of the ζ-potential of mica on the coverage of spheroidal particles for $I = 10^{-3}$ M, and 0.15 M NaCl, respectively. The solid lines show the theoretical results calculated from eqs 12 and 13.

abruptly increased with the particle coverage changing its sign at $\Theta = 0.15$ and 0.2 for the spheres and the spheroids, respectively. Afterward, for exceeding the coverage of 0.3, the plateau ζ-potentials were attained equal to 28 and 20 mV, respectively. Analogous trends were observed for ionic strength of 10^{-3} and 0.15 M, see Figure 5B,C, respectively.

These experimental data were theoretically interpreted in terms of the electrokinetic model developed in refs 66−68, representing a generalization of the Smoluchowski approach to heterogeneous surfaces covered by the particle layer. Because of the presence of deposited particles, the shear flow rate at the interface is decreased, which results in the decrease in the streaming current. Additionally, compared to bare surfaces, there appears a contribution to the streaming current that originates from the electric double layer surrounding the particles. Both of these effects were quantitatively analyzed by solving the nonlinear Navier−Stokes equation applying the multipole expansion method.[69] In the case of thin electric double layers, where $\kappa a \gg 1$ (this parameter was equal to 160 for the experimental conditions shown in Figure 5) the following expression for the ζ-potential of particle-covered surfaces was formulated in ref 68

$$\zeta(\Theta) = F_i(\Theta)\zeta_i + F_p(\Theta)\zeta_p \tag{12}$$

where $\zeta(\Theta)$ is the ζ-potential of the particle layer, ζ_i is the ζ-potential of the bare interface, $F_i(\Theta)$ and $F_p(\Theta)$ are the dimensionless functions, and ζ_p is the ζ-potential of the particles in the bulk.

The $F_i(\Theta)$ function accounts for the decreased flow rate in the vicinity of the interface due to adsorbed particles and the $F_p(\Theta)$ function characterizes the magnitude of the streaming current generated by particles. In the case of spherical particles, these functions were numerically calculated for a broad range of particle coverage and various structures of the particle layers, comprising the RSA, the random, and the equilibrium ones. The exact numerical results were interpolated by the following fitting functions[49]

$$F_i(\Theta) = e^{-C_i^0\Theta}$$
$$F_p(\Theta) = \frac{1}{\sqrt{2}}(1 - e^{-\sqrt{2}C_p^0\Theta}) \tag{13}$$

where $C_i^0 = 10.2$ and $C_p^0 = 6.51$ are the first-order expansion coefficients.

In ref 70 a more exact (for large coverages) fit of the $F_p(\Theta)$ function was given

$$F_p(\Theta) = 0.202\Theta + 0.618(1 - e^{-C_i^0\Theta}) \tag{14}$$

Equation 13 indicates that the contribution to the streaming potential due to the interface exponentially decreases with particle coverage, whereas the contribution due to the deposited particle attains the limiting value of 0.71. The theoretical results calculated from eq 13 for spheres, shown as a red solid line in Figure 5A, agree with the experimental data derived from the streaming potential measurements for the entire range of particle coverage. Unfortunately, presently there exist no exact theoretical results enabling the explicit formulation of the $F_i(\Theta)$ and $F_p(\Theta)$ functions for spheroidal particles. Therefore, in this work, it was assumed that eq 13 can be used as a reasonable approximation with the C_i^0 and C_p^0 coefficients pertinent to linear strings of touching spherical particles given in refs 66−68. Interestingly, the volume of the string composed of n_s spheres is

https://doi.org/10.1021/acs.jpcc.2c06028
J. Phys. Chem. C 2022, 126, 18550−18559

equal to the volume of a prolate spheroid having a shorter axis length equal to the sphere diameter and the longer axis length n_s times larger. For the spheroids used in our investigation the C_i^0 and C_p^0 coefficients corresponding to $n_s = 5$ were equal to 6.5 and 4.0, respectively. As can be seen in Figure 5, the theoretical results calculated from eq 13 using the above parameters well correlate with the experimental data indicating that the increase in the ζ-potential with the particle coverage is less abrupt for spheroids as compared with spheres.

It is worth mentioning that the good fit of experimental data attained using eq 13 can be exploited for a facile determination of the bulk ζ-potential of particles. This can be realized by converting eq 13 to the following form

$$\zeta_p = \zeta(\Theta)/F_p(\Theta) - [F_i(\Theta)/F_p(\Theta)]\zeta_i \quad (15)$$

This formula indicates that the bulk ζ-potential of particles can be determined by streaming potential measurements upon depositing a particle layer of a known coverage. Interestingly, eq 15 is especially sensitive for the low coverage range, which can be exploited to minimize solute consumption. One can argue that such a procedure could have practical significance for bioparticles, especially bacteria, given that the determination of their ζ-potential using the bulk LDV method is impractical because of their low concentration in the suspension and the tendency to aggregation.

Additionally, such irreversibly bound particle layers can be efficiently characterized with respect to their acid−base properties, especially their isoelectric point, applying the streaming potential measurements. This is illustrated in Figure 6 where the dependence of the ζ-potential of the spheroidal

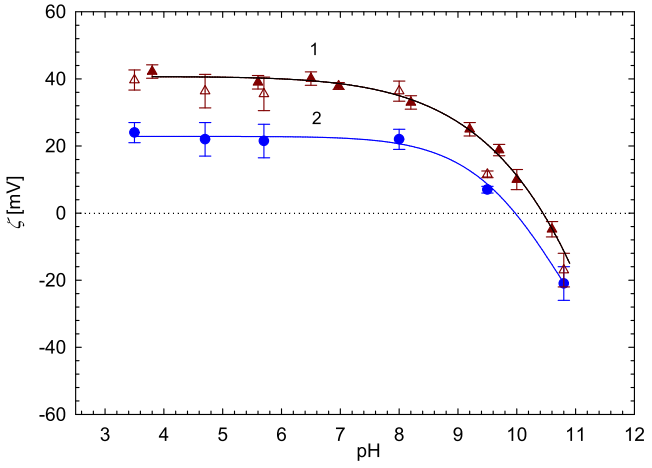

Figure 6. Dependence of the ζ-potential on pH for the ionic strength of 10^{-2} M: 1 the bulk ζ-potential of spheroidal particles derived from LDV (triangles): 2 the spheroidal particle layer (at the particle coverage equal to 0.44) derived from streaming potential measurements (full circles). The empty triangles represent the experimental data recalculated using eq 15. The solid lines are the guide to the eye.

particle layer on pH acquired at an ionic strength of 10^{-2} M is shown. These primary experimental data were converted to the bulk ζ-potential using eq 15 and are shown in Figure 6. As can be seen, they reasonably well agree with the bulk LDV measurements.

Considering that the experimental results obtained in this work confirmed the validity of eqs 3 and 12, they can be used to efficiently predict the ζ-potential of heterogeneous (particle-covered) surfaces. This is illustrated in Figure 7 where the

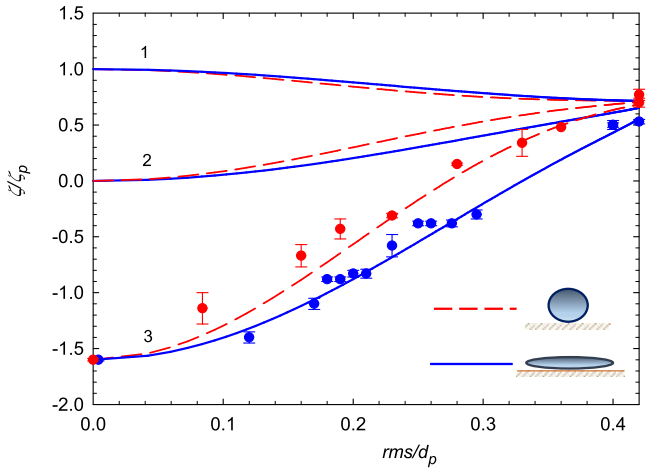

Figure 7. Dependence of the scaled ζ-potential ζ/ζ_p on the scaled rms/d_p for surfaces covered by particle layers; (1) the same sign of particle and substrate ζ-potentials $\zeta_i/\zeta_p = 1$, (2) particles deposited at neutral substrates, $\zeta_i/\zeta_p = 0$, and (3) opposite sign of the particle and the substrate potentials, $\zeta_i/\zeta_p = -1.6$.

dependencies of the scaled ζ-potential of particle-covered surfaces $\zeta(\Theta)/\zeta_p$ calculated from eq 12 on the scaled rms/d_p parameter are shown for spheres and spheroids. The particle coverage corresponding to a given rms in eq 12 was calculated by the inversion of eq 3, which resulted in the following formula

$$\Theta = 0.51\left\{1 \pm \left[1 - 5.536\left(\frac{\text{rms}}{d_p}\right)^2\right]^{1/2}\right\} \quad (16)$$

where the minus sign denotes the range of the coverage before the minimum, where $\Theta < 0.51$.

The solid blue line denotes the theoretical results calculated from eq 12 for spheroidal particles and the dashed red lines show the results calculated for spherical particles. The blue points denote the experimental results obtained for spheroidal particles: pH 5.6, ionic strength 10^{-2} M, $\zeta_p = 40$ mV, $\zeta_i = -64$ mV, and $\zeta_i/\zeta_p = -1.6$. The red points denote the experimental results obtained for spherical particles: pH 5.6, ionic strength 0.01 M, $\zeta_p = 42$ mV, $\zeta_i = -66$ mV, and $\zeta_i/\zeta_p = -1.6$

The theoretical results calculated in this way for various ζ_i/ζ_p are shown in Figure 7 with blue solid lines corresponding to the surfaces covered by spheroids and the dashed red lines corresponding to spherical surface features. The case of $\zeta_i/\zeta_p = 1$ (curves number 1) corresponds to an electrostatically homogeneous surface where both the substrate and the particles bear equal potentials, hence the change in the ζ-potential is solely due to the surface geometrical heterogeneity (roughness). This case was analyzed in ref 70 although the rms parameter was not simultaneously determined. As can be seen in Figure 7, the scaled ζ-potential monotonically decreased with the roughness parameter reaching 0.70 for rms/d_p > 0.3. Interestingly, this effect was practically identical for surfaces covered with spheres and prolate spheroids with an axis ratio of 5. It should also be mentioned that this conclusion is valid for the arbitrary ζ-potential of the particle both with respect to the magnitude and the sign. Therefore, one can expect that the decrease in the rough surface ζ-potential is a universal phenomenon, although a definite conclusion requires further theoretical and experimental studies.

https://doi.org/10.1021/acs.jpcc.2c06028
J. Phys. Chem. C 2022, 126, 18550−18559

The interesting case of heterogeneous surface created by the deposition of charged particles at electrically neutral substrates, where $\zeta_i/\zeta_p = 0$, is depicted in Figure 7 by line number 2. As before, the limiting value of the normalized ζ-potential for spheres and spheroids approached 0.70 for rms/d_p exceeding 0.4.

More pronounced differences appear for $\zeta_i/\zeta_p = -1.6$ experimentally studied in this work (curve 3 in Figure 7). As can be seen, the limiting value of the scaled ζ-potential equal to 0.70 is attained at a faster rate for spheres, practically for rms/d_p larger than 0.4, whereas for spheroids the scaled ζ-potential approached 0.5 for an rms/d_p of 0.4. Interestingly, in this case, the theoretical data agree within experimental error bounds with the experimental results derived from the AFM and the streaming potential measurements.

One can expect that the results shown in Figure 7, which cover the entire range of experimentally accessible particle coverage, can be exploited as useful reference data for the prediction of the ζ-potential of heterogeneous and rough substrates.

4. CONCLUSIONS

An efficient method developed in this work enabled the synthesis of large quantities of monodisperse spheroidal particles exhibiting a positive ζ-potential, which promoted their irreversible deposition at bare, negatively charged interfaces. The particles were thoroughly characterized with respect to their size, shape, electrophoretic mobility, ζ-potential, diffusion coefficient, and hydrodynamic diameter. Interestingly, the shape and the aspect ratio parameter of the particles are comparable to the shape of common bacterial strains, such as *E. coli*, *S. alaskensis*, and *H. gracilis*.

The deposition kinetics of the particles was determined by AFM and adequately interpreted using the random sequential adsorption model. Additionally, the rms parameter of the particle layer was determined for a broad range of coverage and theoretically interpreted in terms of the topographical model developed in this work. These measurements confirmed the side-on deposition mechanism of the particles.

The streaming potential measurements allowed the determination of the ζ-potential of particle layers as a function of their coverage. The experiments were successfully interpreted in terms of the electrokinetic model, using eq 12. The inversion of this equation can be exploited to determine spheroidal particle coverage in situ via the streaming potential measurements. Alternatively, if the particle coverage is known, the streaming potential measurements make it possible to determine the ζ-potential of bioparticles in a more efficient way than using the bulk electrophoretic mobility methods.

The experimental results obtained in this work also allowed us to predict the ζ-potential of heterogeneous and rough surfaces. It is shown that the ζ-potential of rough surfaces monotonically decreases with the surface roughness approaching 0.70 of the smooth surface ζ-potential for the scaled rms/d_p parameter larger than 0.3. This effect, physically originating from the decreased shear flow rate in the vicinity of particles forming surface roughness should be universally valid for the arbitrary ζ-potential value and sign.

It can also be argued that the acquired results, in addition to being significant to basic science, can be exploited as useful reference systems for a quantitative interpretation of the bioparticle deposition phenomena at abiotic surfaces.

■ ASSOCIATED CONTENT

Supporting Information

The Supporting Information is available free of charge at https://pubs.acs.org/doi/10.1021/acs.jpcc.2c06028.

Synthesis of and physicochemical characteristics of the P(S/PGL) particles, calculations of the rms for spheroidal particle layers, calculation of DLVO energy profiles, and modeling deposition kinetics of particles (PDF)

■ AUTHOR INFORMATION

Corresponding Authors

Maria Morga − *Jerzy Haber Institute of Catalysis and Surface Chemistry, Polish Academy of Sciences, 30-239 Krakow, Poland*; orcid.org/0000-0002-4913-9244; Email: maria.morga@ikifp.edu.pl

Zbigniew Adamczyk − *Jerzy Haber Institute of Catalysis and Surface Chemistry, Polish Academy of Sciences, 30-239 Krakow, Poland*; Email: zbigniew.adamczyk@ikifp.edu.pl

Authors

Małgorzata Nattich-Rak − *Jerzy Haber Institute of Catalysis and Surface Chemistry, Polish Academy of Sciences, 30-239 Krakow, Poland*

Damian Mickiewicz − *Centre of Molecular and Macromolecular Studies, Polish Academy of Sciences, 90-363 Lodz, Poland*

Mariusz Gadzinowski − *Centre of Molecular and Macromolecular Studies, Polish Academy of Sciences, 90-363 Lodz, Poland*

Teresa Basinska − *Centre of Molecular and Macromolecular Studies, Polish Academy of Sciences, 90-363 Lodz, Poland*; orcid.org/0000-0002-8429-9665

Complete contact information is available at: https://pubs.acs.org/10.1021/acs.jpcc.2c06028

Notes

The authors declare no competing financial interest.

■ ACKNOWLEDGMENTS

This work was financially supported by the Statutory activity of the Jerzy Haber Institute of Catalysis and Surface Chemistry PAS (theoretical modeling, streaming potential, and AFM measurements) and partially by the Research Project of the National Science Center (Poland) UMO-2018/29/BST8/01721 (synthesis of the PS/PGL spheroidal particles). The authors are deeply indebted to Maja Motyczyńska for invaluable help in preparing the manuscript and the artwork.

■ REFERENCES

(1) Park, S. I.; Song, H.-M. Synthesis of Prolate-Shaped Au Nanoparticles and Au Nanoprisms and Study of Catalytic Reduction Reactions of 4-Nitrophenol. *ACS Omega* **2019**, *4*, 7874−7883.

(2) Pol, V. G.; Calderon-Moreno, J. M.; Chupas, P. J.; Winans, R. E.; Thiyagarajan, P. Synthesis of Monodispersed Prolate Spheroid Shaped Paramagnetic Carbon. *Carbon* **2009**, *47*, 1050−1055.

(3) Wu, L.; Gao, B.; Tian, Y.; Muñoz-Carpena, R.; Zigler, K. J. DLVO Interactions of Carbon Nanotubes with Isotropic Planar Surfaces. *Langmuir* **2013**, *29*, 3976−3988.

(4) Gomez-Flores, A.; Bradford, S. A.; Wu, L.; Kim, H. Interaction Energies for Hollow and Solid Cylinders: Role of Aspect Ratio and Particle Orientation. *Colloids Surf., A* **2019**, *580*, No. 123781.

(5) van Kats, C. M.; Johnson, P. M.; van den Meerakker, J. E. A. M.; van Blaaderen, A. Synthesis of Monodisperse High-Aspect-Ratio Colloidal Silicon and Silica Rods. *Langmuir* **2004**, *20*, 11201−11207.
(6) Kuijk, A.; van Blaaderen, A.; Imhof, A. Synthesis of Monodisperse, Rodlike Silica Colloids with Tunable Aspect Ratio. *J. Am. Chem. Soc.* **2011**, *133*, 2346−2349.
(7) Kuijk, A.; Imhof, A.; Verkuijlen, M. H. W.; Besseling, T. H.; van Eck, E. R. H.; van Blaaderen, A. Colloidal Silica Rods: Material Properties and Fluorescent Labeling. *Part. Part. Syst. Charact.* **2014**, *31*, 706−713.
(8) Bakker, H. E.; Besseling, T. H.; Wijnhoven, J. E. G. J.; Helfferich, P. H.; van Blaaderen, A.; Imhof, A. Microelectrophoresis of Silica Rods Using Confocal Microscopy. *Langmuir* **2017**, *33*, 881−890.
(9) Ho, C. C.; Keller, A.; Odell, J. A.; Ottewill, R. H. Preparation of Monodisperse Ellipsoidal Polystyrene Particles. *Colloids Polym. Sci.* **1993**, *271*, 469−479.
(10) Champion, J. A.; Katare, Y. K.; Mitragotri, S. Making Polymeric Micro- and Nanoparticles of Complex Shapes. *Proc. Natl. Acad. Sci. U.S.A.* **2007**, *104*, 11901−11904.
(11) Morga, M.; Adamczyk, Z.; Basinska, T.; Komar, P.; Gosecka, M.; Żeliszewska, P.; Wasilewska, M. Spheroidal Microparticle Monolayers Characterized by Streaming Potential Measurements. *Langmuir* **2017**, *33*, 9916−9925.
(12) Gadzinowski, M.; Mickiewicz, D.; Basinska, T. Spherical versus Prolate Spheroidal Particles in Biosciences: Does the Shape Make a Difference? *Polym. Adv. Technol.* **2021**, *32*, 3867−3876.
(13) Ortega, A.; García de la Torre, J. Equivalent Radii and Ratios of Radii from Solution Properties as Indicators of Macromolecular Conformation, Shape, and Flexibility. *Biomacromolecules* **2007**, *8*, 2464−2475.
(14) Borkovec, M.; Papastavrou, G. Interactions between Solid Surfaces with Adsorbed Polyelectrolytes of Opposite Charge. *Curr. Opin. Colloid Interface Sci.* **2008**, *13*, 429−437.
(15) Visaveliya, N.; Köhler, J. M. Single-Step Microfluidic Synthesis of Various Nonspherical Polymer Nanoparticles via in Situ Assembling: Dominating Role of Polyelectrolytes Molecules. *ACS Appl. Mater. Interfaces* **2014**, *6*, 11254−11264.
(16) Kosior, D.; Morga, M.; Maroni, P.; Cieśla, M.; Adamczyk, Z. Formation of Poly-L-Lysine Monolayers on Silica: Modeling and Experimental Studies. *J. Phys. Chem. C* **2020**, *124*, 4571−4581.
(17) Tirado, M. M.; Martínez, C. L.; de la Torre, J. G. Comparison of Theories for the Translational and Rotational Diffusion Coefficients of Rod-like Macromolecules. Application to Short DNA Fragments. *J. Chem. Phys.* **1984**, *81*, 2047−2052.
(18) Allison, S. A.; Mazur, S. Modeling the Free Solution Electrophoretic Mobility of Short DNA Fragments. *Biopolymers* **1998**, *46*, 359−373.
(19) Liu, L.; Guo, Z.; Huang, Z.; Zhuang, J.; Yang, W. Size-Selective Separation of DNA Fragments by Using Lysine-Functionalized Silica Particles. *Sci. Rep.* **2016**, *6*, No. 22029.
(20) Clifton, L. A.; Sanders, M. R.; Castelletto, V.; Rogers, S. E.; Heenan, R. K.; Neylon, C.; Frazier, R. A.; Green, R. J. Puroindoline-a, a Lipid Binding Protein from Common Wheat, Spontaneously Forms Prolate Protein Micelles in Solution. *Phys. Chem. Chem. Phys.* **2011**, *13*, 8881−8888.
(21) Sha, J.; Si, W.; Xu, B.; Zhang, S.; Li, K.; Lin, K.; Shi, H.; Chen, Y. Identification of Spherical and Nonspherical Proteins by a Solid-State Nanopore. *Anal. Chem.* **2018**, *90*, 13826−13831.
(22) Dogic, Z.; Fraden, S. Ordered Phases of Filamentous Viruses. *Curr. Opin. Colloid Interface Sci.* **2006**, *11*, 47−55.
(23) Buitenhuis, J. Electrophoresis of Fd-Virus Particles: Experiments and an Analysis of the Effect of Finite Rod Lengths. *Langmuir* **2012**, *28*, 13354−13363.
(24) Young, K. D. The Selective Value of Bacterial Shape. *Microbiol. Mol. Biol. Rev.* **2006**, *70*, 660−703.
(25) Koch, A. L. Shapes That Escherichia Coli Cells Can Achieve, as a Paradigm for Other Bacteria. *Crit. Rev. Microbiol.* **2005**, *31*, 183−190.
(26) Wang, Y.; Hammes, F.; Boon, N.; Egli, T. Quantification of the Filterability of Freshwater Bacteria through 0.45, 0.22, and 0.1 Mm Pore Size Filters and Shape-Dependent Enrichment of Filterable Bacterial Communities. *Environ. Sci. Technol.* **2007**, *41*, 7080−7086.
(27) Wang, Y.; Hammes, F.; Düggelin, M.; Egli, T. Influence of Size, Shape, and Flexibility on Bacterial Passage through Micropore Membrane Filters. *Environ. Sci. Technol.* **2008**, *42*, 6749−6754.
(28) Nattich-Rak, M.; Adamczyk, Z.; Kujda, M. Revealing Deposition Mechanism of Colloid Particles on Human Serum Albumin Monolayers. *Colloids Surf., B* **2016**, *137*, 176−182.
(29) Pelliccione, M.; Karabacak, T.; Gaire, C.; Wang, G.-C.; Lu, T.-M. Mound Formation in Surface Growth under Shadowing. *Phys. Rev. B* **2006**, *74*, No. 125420.
(30) Klapetek, P.; Valtr, M.; Nečas, D.; Salyk, O.; Dzik, P. Atomic Force Microscopy Analysis of Nanoparticles in Non-Ideal Conditions. *Nanoscale Res. Lett.* **2011**, *6*, 514.
(31) Oćwieja, M.; Adamczyk, Z.; Morga, M.; Bielańska, E.; Węgrzynowicz, A. Hematite Nanoparticle Monolayers on Mica Preparation by Controlled Self-Assembly. *J. Colloid Interface Sci.* **2012**, *386*, 51−59.
(32) Shateri Khalil-Abad, M.; Yazdanshenas, M. E.; Nateghi, M. R. Effect of Cationization on Adsorption of Silver Nanoparticles on Cotton Surfaces and Its Antibacterial Activity. *Cellulose* **2009**, *16*, 1147−1157.
(33) Morga, M.; Adamczyk, Z.; Oćwieja, M.; Bielańska, E. Hematite/Silver Nanoparticle Bilayers on Mica − AFM, SEM and Streaming Potential Studies. *J. Colloid Interface Sci.* **2014**, *424*, 75−83.
(34) Oćwieja, M.; Adamczyk, Z.; Morga, M.; Kubiak, K. Influence of Supporting Polyelectrolyte Layers on the Coverage and Stability of Silver Nanoparticle Coatings. *J. Colloid Interface Sci.* **2015**, *445*, 205−212.
(35) Bortchagovsky, E. G.; Mishakova, T. O.; Hingerl, K. Ellipsometry of Monolayers of Metallic Nanoparticles Taking into Account Depolarization. *Thin Solid Films* **2014**, *571*, 625−630.
(36) Battie, Y.; Izquierdo-Lorenzo, I.; Resano-Garcia, A.; Naciri, A. E.; Akil, S.; Adam, P. M.; Jradi, S. Determination of Gold Nanoparticle Shape from Absorption Spectroscopy and Ellipsometry. *Appl. Surf. Sci.* **2017**, *421*, 301−309.
(37) Yang, Y.; Knust, S.; Schwiderek, S.; Qin, Q.; Yun, Q.; Grundmeier, G.; Keller, A. Protein Adsorption at Nanorough Titanium Oxide Surfaces: The Importance of Surface Statistical Parameters beyond Surface Roughness. *Nanomaterials* **2021**, *11*, 357.
(38) Kosior, D.; Maroni, P.; Borkovec, M. Particle Deposition to Silica Surfaces Functionalized with Cationic Polyelectrolytes. *Colloids Interfaces* **2021**, *5*, 26.
(39) Kosior, D.; Gvaramia, M.; J Scarratt, L. R.; Maroni, P.; Trefalt, G.; Borkovec, M. Thickness of the Particle-Free Layer near Charged Interfaces in Suspensions of like-Charged Nanoparticles. *Soft Matter* **2021**, *17*, 6212−6224.
(40) Olsson, A. L. J.; Quevedo, I. R.; He, D.; Basnet, M.; Tufenkji, N. Using the Quartz Crystal Microbalance with Dissipation Monitoring to Evaluate the Size of Nanoparticles Deposited on Surfaces. *ACS Nano* **2013**, *7*, 7833−7843.
(41) Seymour, M. B.; Chen, G.; Su, C.; Li, Y. Transport and Retention of Colloids in Porous Media: Does Shape Really Matter. *Environ. Sci. Technol.* **2013**, *47*, 8391−8398.
(42) Tarnapolsky, A.; Freger, V. Modeling QCM-D Response to Deposition and Attachment of Microparticles and Living Cells. *Anal. Chem.* **2018**, *90*, 13960−13968.
(43) Adamczyk, Z.; Sadowska, M.; Żeliszewska, P. Applicability of QCM-D for Quantitative Measurements of Nano- and Microparticle Deposition Kinetics: Theoretical Modeling and Experiments. *Anal. Chem.* **2020**, *92*, 15087−15095.
(44) Salerno, M. B.; Flamm, M.; Logan, B. E.; Velegol, D. Transport of Rodlike Colloids through Packed Beds. *Environ. Sci. Technol.* **2006**, *40*, 6336−6340.
(45) Weiss, T. H.; Mills, A. L.; Hornberger, G. M.; Herman, J. S. Effect of Bacterial Cell Shape on Transport of Bacteria in Porous Media. *Environ. Sci. Technol.* **1995**, *29*, 1737−1740.
(46) Xu, S.; Liao, Q.; Saiers, J. E. Straining of Nonspherical Colloids in Saturated Porous Media. *Environ. Sci. Technol.* **2008**, *42*, 771−778.

https://doi.org/10.1021/acs.jpcc.2c06028
J. Phys. Chem. C 2022, 126, 18550−18559

(47) Liu, Q.; Lazouskaya, V.; He, Q.; Jin, Y. Effect of Particle Shape on Colloid Retention and Release in Saturated Porous Media. *J. Environ. Qual.* **2010**, *39*, 500−508.
(48) Adamczyk, Z.; Pomorska, A.; Sadowska, M.; Nattich-Rak, M.; Morga, M.; Basinska, T.; Mickiewicz, D.; Gadzinowski, M. QCM-D Investigations of Anisotropic Particle Deposition Kinetics: Evidences of the Hydrodynamic Slip Mechanisms. *Anal. Chem.* **2022**, *94*, 10234−10244.
(49) Zembala, M.; Adamczyk, Z.; Warszyński, P. Streaming Potential of Mica Covered by Latex Particles. *Colloids Surf., A* **2003**, *222*, 329−339.
(50) Adamczyk, Z.; Nattich, M.; Wasilewska, M.; Zaucha, M. Colloid Particle and Protein Deposition - Electrokinetic Studies. *Adv. Colloid Interface Sci.* **2011**, *168*, 3−28.
(51) Sofińska, K.; Adamczyk, Z.; Kujda, M.; Nattich-Rak, M. Recombinant Albumin Monolayers on Latex Particles. *Langmuir* **2014**, *30*, 250−258.
(52) Morga, M.; Adamczyk, Z.; Kosior, D. Silica Nanoparticle Monolayers on a Macroion Modified Surface: Formation Mechanism and Stability. *Phys. Chem. Chem. Phys.* **2017**, *19*, 22721−22732.
(53) Morga, M.; Adamczyk, Z.; Kosior, D.; Oćwieja, M. Hematite/Silica Nanoparticle Bilayers on Mica: AFM and Electrokinetic Characterization. *Phys. Chem. Chem. Phys.* **2018**, *20*, 15368−15379.
(54) Oćwieja, M.; Morga, M. Electrokinetic Properties of Cysteine-Stabilized Silver Nanoparticles Dispersed in Suspensions and Deposited on Solid Surfaces in the Form of Monolayers. *Electrochim. Acta* **2019**, *297*, 1000−1010.
(55) Einstein, A. Theorie Der Opaleszenz von Homogenen Flüssigkeiten Und Flüssigkeitsgemischen in Der Nähe Des Kritischen Zustandes. *Ann. Phys.* **1910**, *338*, 1275−1298.
(56) Oshima, H.; Furusawa, K. *Electrical Phenomena at Interfaces: Fundamentals, Measurements, and Applications*; Marcel Dekker, Inc.: New York, 1998.
(57) Adamczyk, Z.; Morga, M.; Nattich-Rak, M.; Sadowska, M. Nanoparticle and Bioparticle Deposition Kinetics. *Adv. Colloid Interface Sci.* **2022**, *302*, No. 102630.
(58) Zembala, M.; Adamczyk, Z. Measurements of Streaming Potential for Mica Covered by Colloid Particles. *Langmuir* **2000**, *16*, 1593−1601.
(59) Ohshima, H. Approximate Analytic Expression for the Electrophoretic Mobility of Moderately Charged Cylindrical Colloidal Particles. *Langmuir* **2015**, *31*, 13633−13638.
(60) Ohshima, H. Henry's Function for Electrophoresis of a Cylindrical Colloidal Particle. *J. Colloid Interface Sci.* **1996**, *180*, 299−301.
(61) Scales, P. J.; Grieser, F.; Healy, T. W. Electrokinetics of the Muscovite Mica-Aqueous Solution Interface. *Langmuir* **1990**, *6*, 582−589.
(62) Kujda, M.; Adamczyk, Z.; Cieśla, M. Monolayers of the HSA Dimer on Polymeric Microparticles-Electrokinetic Characteristics. *Colloids Surf., B* **2016**, *148*, 229−237.
(63) Michna, A.; Adamczyk, Z.; Sofińska, K.; Matusik, K. Monolayers of Poly(Amido Amine) Dendrimers on Mica − In Situ Streaming Potential Measurements. *J. Colloid Interface Sci.* **2017**, *485*, 232−241.
(64) Michna, A.; Adamczyk, Z.; Siwek, B.; Oćwieja, M. Silver Nanoparticle Monolayers on Poly(Ethylene Imine) Covered Mica Produced by Colloidal Self-Assembly. *J. Colloid Interface Sci.* **2010**, *345*, 187−193.
(65) Adamczyk, Z. *Particles at Interfaces: Interactions, Deposition, Structure*; Elsevier: London, 2017.
(66) Adamczyk, Z.; Warszyński, P.; Zembala, M. Influence of Adsorbed Colloid Particles on Streaming Potential. *Bull. Pol. Acad. Sci.* **1999**, *47*, 239−258.
(67) Adamczyk, Z.; Sadlej, K.; Wajnryb, E.; Nattich, M.; Ekiel-Jeżewska, M. L.; Bławzdziewicz, J. Streaming Potential Studies of Colloid, Polyelectrolyte and Protein Deposition. *Adv. Colloid Interface Sci.* **2010**, *153*, 1−29.
(68) Sadlej, K.; Wajnryb, E.; Bławzdziewicz, J.; Ekiel-Jeżewska, M. L.; Adamczyk, Z. Streaming Current and Streaming Potential for Particle Covered Surfaces: Virial Expansion and Simulations. *J. Chem. Phys.* **2009**, *130*, No. 144706.
(69) Ekiel-Jeżewska, M. L.; Sadlej, K.; Wajnryb, E. Friction of Rodlike Particles Adsorbed to a Planar Surface in Shear Flow. *J. Chem. Phys.* **2008**, *129*, No. 041104.
(70) Ekiel-Jeżewska, M. L.; Adamczyk, Z.; Bławzdziewicz, J. Streaming Current and Effective ζ-Potential for Particle-Covered Surfaces with Random Particle Distributions. *J. Phys. Chem. C* **2019**, *123*, 3517−3531.

https://doi.org/10.1021/acs.jpcc.2c06028
J. Phys. Chem. C 2022, 126, 18550−18559